Enhanced Differential Power Processor for PV Systems: Resonant Switched-Capacitor Gyrator Converter With Local MPPT

Alon Blumenfeld, *Student Member, IEEE*, Alon Cervera, *Student Member, IEEE*, and Mor Mordechai Peretz, *Member, IEEE*

***Abstract*— This paper introduces an enhanced differential power processor topology and principle of operation for photovoltaic (PV) systems that is based on switched-capacitor technology, featuring local maximum power point tracking (MPPT) capability, zero current switching, high efficiency over wide-operation range, and reduced size. The new converter operates as a voltage-dependent current-source and is regulated by dead-time or frequency control. Local MPPT on the individual PV elements is realized and the operation is demonstrated by simulation and experiments. Differential power processing operation is verified using 150-W prototypes, demonstrating ultimate improvement in the power harvesting capability of above 90% and up to 99% out of the available power in the string, under different insolation levels.**

***Index Terms*— Differential power processing, digital control, gyrator, local control, maximum power point tracking (MPPT), photovoltaic power, renewable energy.**

I. Introduction

FULL or partial shading of a serially connected photovoltaic (PV) string severely impacts the power that can be extracted from it [1], [2]. In general, two groups of power processing solutions have been proposed to remedy the shading problem. One group is based on a dedicated converter/inverter per element [3]–[5], whereas the other group of solutions keeps the series connection of the elements intact, and process mismatched currents due to the shaded unit(s) using parallel circuitry [6]–[8], where [9] presents a comparison between these methods. The latter has the advantage of processing only the power differences between the PV elements, thus minimizes conversion losses and improves reliability. This architecture, referred as differential power processing [10], is the subject of this paper.

A unique advantage of the differential power processing architecture is that maximum power point tracking (MPPT) can be obtained locally, in the PV element level, by processing only the necessary amount of power needed to achieve maximum power point (MPP). Several converter realizations have been proposed as candidates as differential power processors (DPPs), mainly derived from battery management applications [11], [12]. A switched capacitor converter (SCC) proposed in [13] and [14], as a voltage equalizer with simple open-loop control, relying on the assumption that MPP voltage deviation due to change in irradiance level is negligibly small. This approach stands out in its simplicity, high self-efficiency and lower cost. However, it lacks MPPT capability without introducing losses. A buck-boost topology has also been proposed, acting as an equalizer [8], and further developed in [10] to obtain local MPPT by differential processing to keep all PV units in MPP. However, compared with SCC technology of the same power level, it is bulkier in volume due to the large magnetic element required [15]. Furthermore, the MPP voltage of a PV element variation as a function of the irradiance is affected by the element's internal resistance and temperature. The resultant voltage drift may be either negative or positive with respect to the nominal MPP [16], [17], which highlights the need for a DPP with true tracking capabilities, i.e., step-up/down functionality.

This paper introduces an enhanced DPP topology that incorporates the virtues of both worlds in a newly developed current

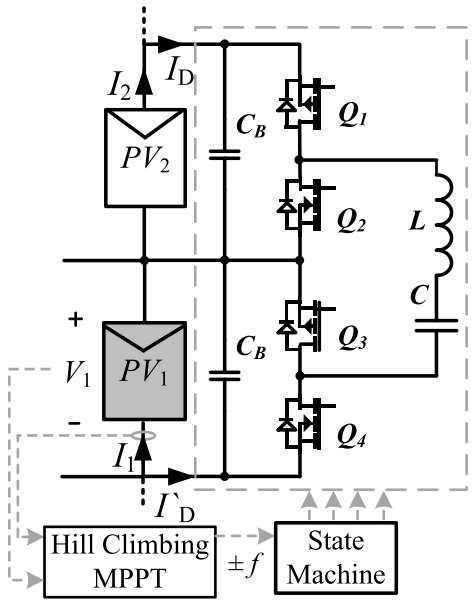

Fig. 1. DPP conceptual hardware setup.

Manuscript received January 31, 2014; revised April 13, 2014; accepted May 27, 2014. Date of publication June 17, 2014; date of current version October 29, 2014. Recommended for publication by Associate Editor Yen-Shin Lai.

The authors are with the Power Electronics Laboratory, Department of Electrical and Computer Engineering, Ben-Gurion University of the Negev, Beer-Sheva 78718, Israel (e-mail: alonblu@bgu.ac.il; cervera@bgu.ac.il; morp@ee.bgu.ac.il).

Color versions of one or more of the figures in this paper are available online at http://ieeexplore.ieee.org.

Digital Object Identifier 10.1109/JESTPE.2014.2331277

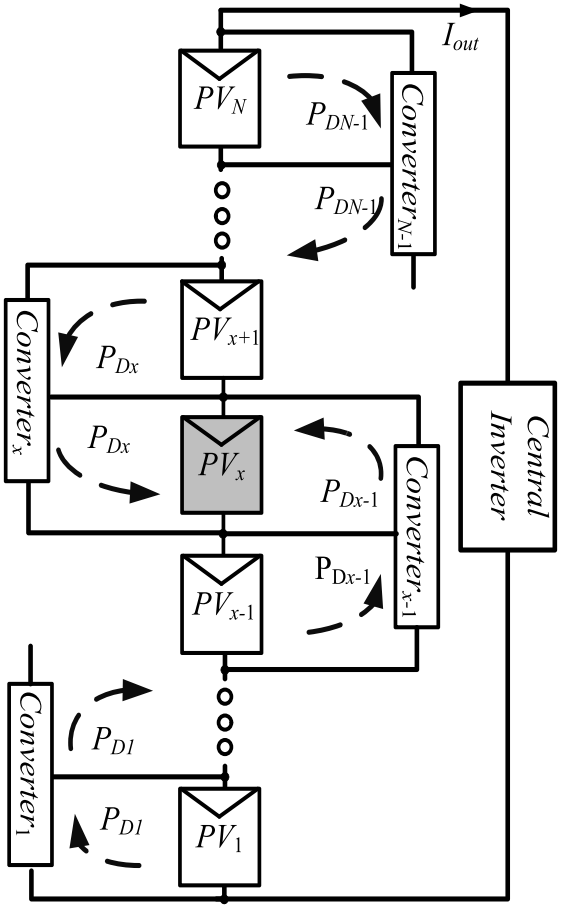

Fig. 2. Example of the power flow for a N PV panel string connected to $N-1$ gyrator DPPs, containing a shaded PV at the x-location.

sourcing converter that is based on resonant SCC technology (Fig. 1). The new converter is of low-volume, features high-efficiency with extended operation range, and is capable to perform local MPPT. This paper covers a brief introduction to DPP architecture and presents a new converter topology with its principle of operation. Later, differential power processing and local MPPT are described by simulations and experiments.

II. Differential Power Processing—Operation and Realization

The main goal of differential power processing in PV systems is to maximize the power conversion efficiency by processing only a small portion of the power being produced. The concept has been initially introduced in [18] and [19] and further developed and demonstrated in [10]. The architecture is conceptually shown in Fig. 2. It consists of N serially connected PV elements and $N-1$ current sourcing converters connected in parallel with two adjacent PV elements. The differential power passes along the string in a so-called bucket-brigade pattern. Each converter performs local MPPT to one of its two connected PVs by sinking or sourcing current to/from the neighboring PV element. A central grid-connected inverter is still used to interact with the grid and to track the global MPPT. Effectively, it also performs the local MPPT for the N^{th} element.

The differential converters are needed only in case of mismatch in the MPPs, i.e., only a portion of the power is processed. The MPP is maintained for each of the PV elements thanks to differential current provided by the DPP. The amount of power processed by each converter in a string of N elements to bring a mismatched element (PVx, Fig. 2) to its MPP can be expressed as [13]

$$P_{Dj} = \begin{cases} \frac{P_0 - P_s}{N} j; & j < x \\ \frac{P_0 - P_s}{N}(N-j); & j \geq x \end{cases} \tag{1}$$

where the index j represents the location of a converter in the string, P_s is the maximum power of the shaded element, and P_0 is the power of a nonshaded element at its MPP. For better illustration, consider an example of a string with five PV elements and the third element is shaded, then the power processed by the third converter would be $(P_0 - P_s) \times 2/5$. Further details on the distribution of the processed power can be found in [13].

It can be observed from (1) that adjacent converters to the shaded element are required to process most of the power, whereas others located farther in the string contribute a smaller portion of the power, linearly proportional to their location with respect to the mismatched PV element. A current-sourcing converter that operates as a DPP is thus required to be bidirectional and capable of step-up/down operation. In the context of this paper, the harvesting factor, ξ, is defined as the relationship between the total extracted power out of a serially connected string, P_{out}, and the sum of the absolute maximum power that can be harvested from each individual element, $P_{i,\text{MPP}}$, that is

$$\xi = \frac{P_{\text{out}}}{\sum_{i=1}^{N} P_{i,\text{MPP}}}. \tag{2}$$

Considering (1) and (2), it would be highly advantageous that the efficiency of the converter will be independent of the operating conditions. Converter topologies, such as switched-capacitor [12] or buck-boost [10], originally proposed for battery equalization and realized for PV applications have many merits, however, their efficiency range is limited. The SCC lacks MPPT capability [13]. In a buck-boost configuration, the efficiency range is somewhat limited around the nominal power level, and there is a tradeoff between the size and performance of the converter.

To overcome these challenges, this paper introduces a new DPP topology. It combines the benefits of reduced size SCC and current sourcing properties with high efficiency over a wide range [20].

III. Resonant Switched-Capacitor

The converter configuration as a DPP is shown in Fig. 1. Similar to the architecture of a conventional resonant switched capacitor 1:1 converter (RSCC) [21]–[24], the DPP includes four switches and a resonant tank. Two PV elements connect as input and output sources.

As opposed to the operation of a classical SCC that includes a charge state and a discharge state, here, an additional

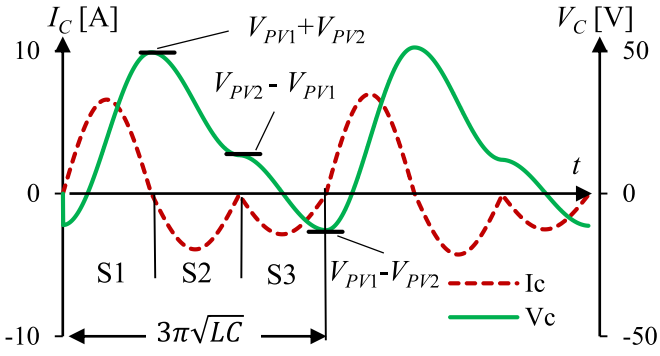

Fig. 3. Typical waveforms (obtained from simulation) of the flying capacitor voltage and current. Circuit parameters are $V_{\mathrm{PV1}} = 20$ V, $V_{\mathrm{PV2}} = 31$ V, $R_s = 0.15\ \Omega$, $L = 5.2\ \mu$H, and $C = 0.25\ \mu$F.

switching phase is introduced that breaks the rigid connection of the input/output voltage gain and the efficiency of the converter. Controlling the sequence of the switches governs the power flow direction, hence bidirectional step-up/down operation.

The operation of the gyrator RSCC (GRSCC), shown in Fig. 1, is described for one steady-state charge/discharge/balance cycle and is assisted by Fig. 3 that shows the capacitor voltage, V_C, and the resonant tank current, I_C, for a case of a MPP mismatch that requires a nonunity step-up conversion. By turning Q_1, Q_3 ON, a charge state (S1) is commenced, which resonantly charges the flying capacitor from PV_2. At zero current, Q_1, Q_3 are turned OFF and Q_2, Q_4 are turned ON (state S2). At this point, the flying capacitor resonantly discharges onto PV_1. If PV_1 voltage, V_{PV1}, and PV_2 voltage, V_{PV2}, are of different values, only a portion of the charge is delivered to the output and results in V_C that is different than its voltage at the starting point of S1. The amount of this voltage difference (neglecting R_s—parasitic resistances in each loop) equals to twice the residual voltage of the flying capacitor. By turning Q_2, Q_3 ON (S3), the resonant tank is short-circuited. This creates the required charge-balance and reverses the flying capacitor voltage polarity such that the voltage at the end of S3 equals to the voltage at the beginning of S1.

The addition of a third, charge balancing state, to the switching sequence transforms the resonant SCC into a voltage dependent current-sourcing converter that, neglecting losses, is capable of accommodating any input to output voltage gain (larger and smaller than unity). It should be noted that the order of the switching sequence will govern the power flow direction.

To facilitate regulation of the amount of charge that is transferred to the output, a pulse density modulation is employed [15], [25], i.e., time-delay is introduced between the charge and the discharge states. The average currents (I_D, I'_D) (Fig. 1) and voltages (V_{PV1}, V_{PV2}) of the converter can be defined as a gyrator relationship [20], [26], [27]

$$I_D = 2fCV_{\mathrm{PV2}}\ ;\ V_{\mathrm{PV1}} = \frac{1}{2fC}I'_D \tag{3}$$

where f is the frequency of a cycle that includes the three states and the time-delay. Maximum differential current is passed when no additional time-delay is added. It can be observed from (3), that the differential current is inversely proportional to the time-delay, but linearly proportional with f.

This implies that controlling the differential current by the frequency as the correction signal is preferred, since variations in the time-delay would result in a nonlinear behavior. Furthermore, the time resolution of a variable frequency signal, generated by a local oscillator, is not constant and strongly depends on the operating point [28], which introduces additional nonlinearity. By modifying the correction signal to frequency, incremented by fixed steps, df, these nonlinearities are eliminated, and the power converter can be treated as a constant gain block from frequency to current as prescribed in (3).

The relationship between the maximum current, $I_{D\max}$, passed from PV_1, and the voltage on an adjacent element, PV_2, is a function of the capacitive and inductive components of the resonant tank (L, C), and can be expressed as

$$I_{D\max} = \frac{2}{3\pi Z}V_{\mathrm{PV2}}\ ;\ Z = \sqrt{L/C}. \tag{4}$$

The output voltage ripple of the converter primarily depends on the ratio between the resonant tank capacitance, C, and the bus capacitance, C_B (in parallel to the PV element), as detailed in [15], $\Delta V_{2,p\text{-}p}$ can be expressed as

$$\Delta V_{2,p\text{-}p} = 2V_1\frac{C}{C_B}\left(1 - \frac{f}{3f_{\max}}\right) \tag{5}$$

where $f_{\max}$ is the maximum operating frequency. Assuming that identical parasitic resistances R_s exist in all three subcircuits (Fig. 1), the expected efficiency of the converter can be estimated by

$$\eta = \left[1 + \frac{\pi}{2}\frac{R_s}{Z}(A + A^{-1} - 1)\right]^{-1}\ ;\ A = \frac{V_{\mathrm{PV2}}}{V_{\mathrm{PV1}}}. \tag{6}$$

To illustrate the efficiency behavior, Fig. 4 shows typical curves that were obtained from (6) of the expected efficiency as a function of A, for various ratios of $Q = Z/R_s$. In addition, [20] investigate the efficiency to current curve and farther analysis of the GRSCC efficiency, where [15] explores the inductor's volume and the input/output voltage ripple. Ideally, assuming negligibly small parasitic resistances, the efficiency of the converter would be 100% for any finite conversion ratio. A unique feature associated hitherto only with switched-inductor converters, is now made available to resonant SCC as well.

IV. Power Flow Control and Local MPPT

In case of MPP mismatch in more than one element in the string, the DPPs are required not only to operate at conversion ratios higher or smaller than unity to transfer the required current difference, but also to control the direction of the current toward the weaker PV element from both sides of the string. The introduced GRSCC, shown in Fig. 1, operates as a current-source and thus is capable of stepping the voltage up or down as required by the load. To deliver power from PV_1 to PV_2 the sequence will be (S1, S2, S3). That is, charge from PV_1, discharge on PV_2, and reverse the flying capacitor

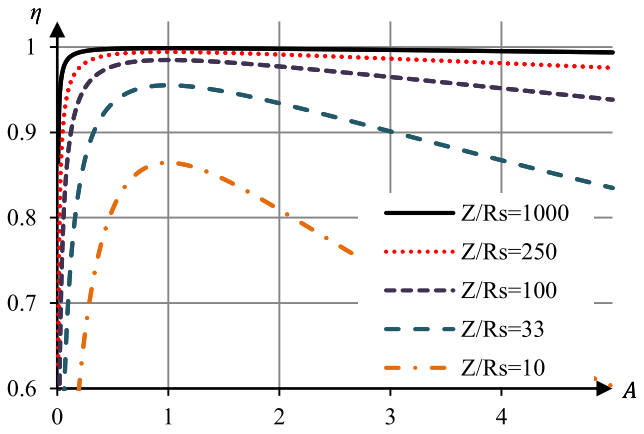

Fig. 4. Theoretical efficiency curves as a function of the voltage gain, A, with normalized loop resistance as a parameter.

polarity. In the case of power to be delivered from PV_2 to PV_1 the sequence will be reversed to (S2, S1, S3).

A. Zero Current Switching

To fully utilize the benefits of the converter, zero current switching (ZCS) for the entire operation range is essential. Since the resonant characteristics may vary significantly with the operating conditions, the simplistic approach of a comparator-based zero current detector is not suitable here. Other direct ZCS methods, such as [29] or [30] have demonstrated wide-operation range, however, they rely on high-performance processors with fast execution rate for proper operation.

To overcome the variations in the operating conditions and rely on limited processing capabilities, an adaptive ZCS control scheme has been developed, based on an accumulative calibration of the switching time. The control scheme applies an analysis of the rectified L–C tank current on areas in vicinity to the transition between switching states (estimated location of the zero crossing point). Instead of sampling multiple points within each cycle in high frequencies, here the current is sampled once or less per cycle, increasing phase shift in relation to the switching cycle. This forms a vector of the current shape in the area of the commutation. This method of operations is allowed assuming that the voltages at the DPP terminals are virtually constant during a calibration cycle, which is much shorter than an MPPT iteration time.

For a calibrated ZCS transition, the rectified current signal should have a V shape with a minimum at zero, centered at the exact switching time. Noncalibrated switching action results in one out of four possible scenarios, as can be shown in Fig. 5 and summarized in Table I, indicating whether the transition has occurred early or late with respect to the actual zero point.

Based on this information, and on the distance between the minimum and transition time, the switching time may be increased or decreased per switching state.

B. MPPT Implementation

Among the wide diversity of possible MPPT algorithms that can be realized using local information [31], the well-known hill-climbing (HC) scheme is chosen [32]. The HC MPPT features a simple realization based on readily available information; it does not require continuous perturbations and its convergence rate to the MPP can be enhanced [32]. In this paper, the developed MPPT algorithm utilizes a similar architecture as in [10] and [33], but is further modified to produces variable step values based on the difference between the PV element's operating point and its MPP. By doing so, faster and more accurate convergence toward the MPP is facilitated. As described earlier, each DPP performs local HC MPPT on one PV element in the string. In this paper, it is set to be carried out on the lower element. The conceptual hardware setup shown in Fig. 1 shows the sensing points for the current and voltage of the PV element. The controller calculates $\mathrm{d}p_{\mathrm{PV}}/\mathrm{d}v_{\mathrm{PV}}$ and $\mathrm{d}p_{\mathrm{PV}}/\mathrm{d}i_{\mathrm{PV}}$ (v_{PV} is the sensed PV voltage, i_{PV} is the sensed PV current, and $p_{\mathrm{PV}} = v_{\mathrm{PV}} \times i_{\mathrm{PV}}$ is the calculated PV power) as the error signals and updates f accordingly. The procedure is repeated until $\mathrm{d}p_{\mathrm{PV}}/\mathrm{d}v_{\mathrm{PV}}$ or $\mathrm{d}p_{\mathrm{PV}}/\mathrm{d}i_{\mathrm{PV}}$ has stabilized in the vicinity of zero, as prescribed by the HC MPPT algorithm. The correction signal $\mathrm{d}p_{\mathrm{PV}}/\mathrm{d}v_{\mathrm{PV}}$ can be expressed as

$$\frac{\mathrm{d}p_{\mathrm{PV}}}{\mathrm{d}v_{\mathrm{PV}}} = i_{\mathrm{PV}} + \frac{\mathrm{d}i_{\mathrm{PV}}}{\mathrm{d}v_{\mathrm{PV}}} v_{\mathrm{PV}} \tag{7}$$

where the other conceivable correction signal $\mathrm{d}p_{\mathrm{PV}}/\mathrm{d}i_{\mathrm{PV}}$ can expressed as

$$\frac{\mathrm{d}p_{\mathrm{PV}}}{\mathrm{d}i_{\mathrm{PV}}} = v_{\mathrm{PV}} + \frac{\mathrm{d}v_{\mathrm{PV}}}{\mathrm{d}i_{\mathrm{PV}}} i_{\mathrm{PV}}. \tag{8}$$

It can be observed from (7) and (8) that different working conditions (such as insolation or temperature levels, which directly affect the PV element's i_{PV} and v_{PV} characteristics) result in a different correction signal. To facilitate uniform

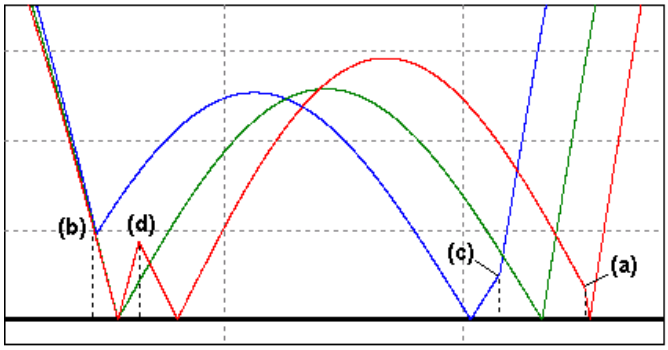

Fig. 5. Waveforms portraying early, exact, and late switching scenarios. (a) Early. (b) Early. (c) Late. (d) Late.

TABLE I
CRITERIA FOR DISTINGUISHING BETWEEN EARLY OR LATE SWITCHING

Reference in Fig. 5	Shape	Minimum location*	Minimum value	Conclusion
(a)	'V'	After	Zero	Early
(b)	'V'	On time	Positive	Early
(c)	'V'	Before	Zero	Late
(d)	'W'	After	Zero	Late

*In relation to the transition time

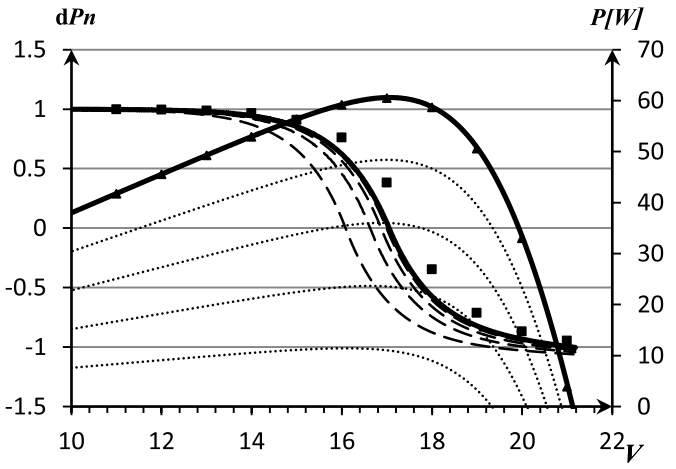

Fig. 6. Typical dp_n and power curves as a function of the panel voltage for various insolation levels.

control, dp_{PV}/dv_{PV} correction signal can be normalized by i_{PV}, whereas dp_{PV}/di_{PV} can be normalized by v_{PV}. The dp_n is designed to obtain a proportional indication of the distance between the working bias point and the MPP. Thus, dp_n is defined as a combination of the two correction signals by appointing normalized dp_{PV}/dv_{PV} for $v_{PV} \le V_{MPP}$ and negative normalized dp_{PV}/di_{PV} for $v_{PV} > V_{MPP}$. Practically the closer to zero absolute value of the two conceivable normalized correction signals is appointed by the control system to be dp_n, the correction signal controlling I_D. The hybrid normalized signal, dp_n can now be expressed as

$$dp_n = \begin{cases} 1 + \frac{di_{PV}}{dv_{PV}} \frac{v_{PV}}{i_{PV}}; & v_{PV} \le V_{MPP} \\ -\left(1 + \frac{dv_{PV}}{di_{PV}} \frac{i_{PV}}{v_{PV}}\right); & v_{PV} > V_{MPP}. \end{cases} \tag{9}$$

Fig. 6 shows typical curves of (9) for a several insolation levels. It can be observed that dp_n holds similar values in different insolation levels and is naturally bounded in $[1, -1]$ interval. The modified HC MPPT is thus designed to generate a variable step in f, proportional to dp_n according to

$$f[n] = f[n-1] + \Delta f_{max} dp_n \tag{10}$$

where $f[n]$ is the current frequency command generated by the controller governing I_D (Fig. 1), $f[n-1]$ is the frequency generated in the previous MPPT iteration and Δf_{max} sets the maximum frequency step that is allowed. The maximum frequency of f is bounded by the GRSCC natural frequency $(3\pi\sqrt{LC})^{-1}$, where no additional delay time is added. The minimum value of f is determined by the size of the digital controlled oscillator (DCO) period register.

The convergence time of the MPPT algorithm and its pattern are primarily dependent on the step size Δf_{max}, which can be viewed as the integral gain factor of (10). For small frequency steps the convergence would be smooth but slow, whereas large frequency steps would result in rapid convergence, but may introduce an oscillating error around the MPP. In this paper, Δf_{max} has been manually selected to produce the fastest convergence, while still maintaining a first-order pattern (i.e., without overshoot).

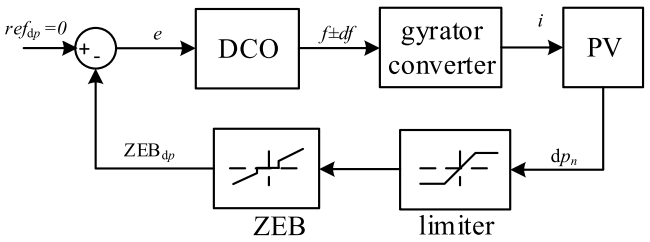

Fig. 7. Block diagram of the DPP digital control system.

C. Resolution Effect on Limit Cycle Oscillations

Convergence of dp_n to zero is impractical due to the discrete nature of f (generated by the digital hardware) and as a consequence dp_n has discrete steps. The resolution of dp_n and f has to be carefully selected to assure stability around MPP, i.e., to avoid limit cycle oscillations [34]. Since dp_n is not sensed directly, a practical way to eliminate such oscillations is to decrease the resolution of the calculated dp_n around zero by introducing a zero error bin (ZEB) of size Δ. The ZEB is defined such that an absolute value of the calculated dp_n less than Δ is considered as zero error, indicating the system has converged to its MPP. The size of Δ should be set such that the ZEB contains at least one value of measurable dp_n (Fig. 6).

The smallest frequency step (1 bit resolution), Δf_{DCO}, that can be generated by the DCO is a function of the time base of the local oscillator, TB, and the running frequency, f_{DCO}. According to [34], Δf_{DCO} can be expressed as

$$\begin{aligned} \Delta f_{DCO} &= \frac{1}{N_{per}TB} - \frac{1}{(N_{per}-1)TB} \approx \frac{1}{N_{per}^3 TB} \\ &= TB f_{DCO}^2 \end{aligned} \tag{11}$$

where N_{per} is the number of TBs in one period.

Around the MPP, the no limit cycles criterion can be expressed as

$$A_{dpi} \times G_{if}(V_{pv2}) \times \Delta f_{DCO} < \Delta; \begin{cases} A_{dpi} = \frac{dp_n}{di_D} \\ G_{if} = \frac{di_D}{df} \end{cases} \tag{12}$$

where A_{dpi} is the PV element small-signal gain between the normalized gradient (dp_n) and the differential current (i_D), which can be obtained by taking the derivative of (9) with respect to i_D, and $G_{if}(V_{pv2})$ is the GRSCC current-to-frequency small signal gain taking the derivative of (3) with respect to f. The block diagram of Fig. 7 shows the control loop of a single GRSCC DPP and the effect of Δf_{DCO} step on dp_n.

The derivatives of A_{dpi} and G_{if} around the maximum power point, which is of interest for limit cycles calculation, can be expressed as a function of the system parameters as

$$A_{dpi}\Big|_{MPP} = \frac{V_{1,MPP}}{I_{1,MPP}}; \; G_{if}\Big|_{MPP} = 2CV_{2,MPP} \tag{13}$$

where $V_{1,MPP}$ and $I_{1,MPP}$ are the controlled PV panel's MPP voltage and current, respectively, $V_{2,MPP}$ is the adjacent PV panel's MPP voltage, and C is the resonant tank capacitance. It should be noted that the derivative of A_{dpi} has been obtained

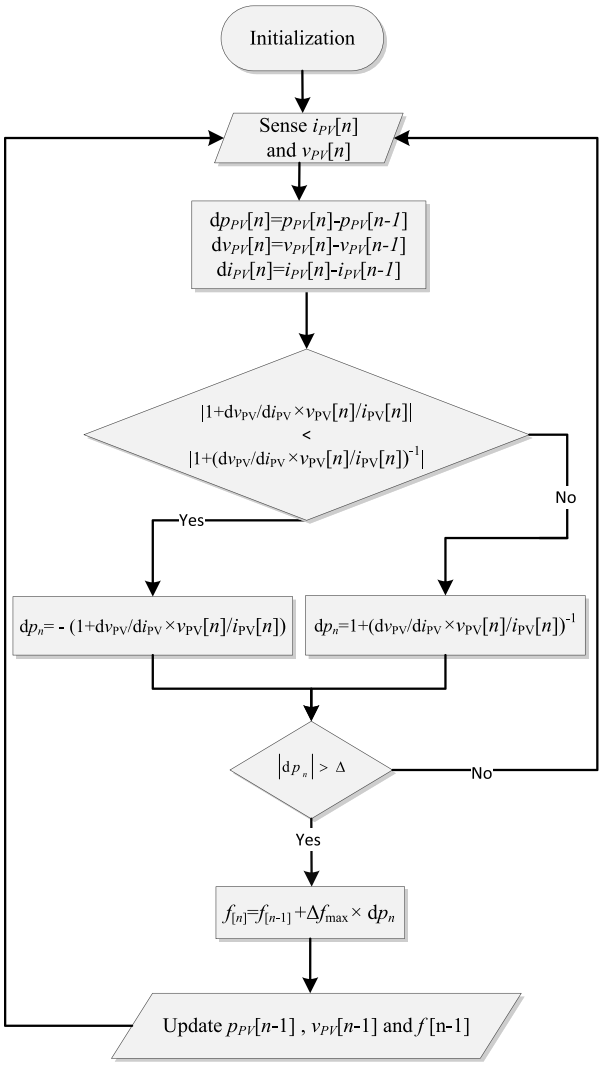

Fig. 8. Flowchart of the modified HC MPPT algorithm.

using a numerical calculation. Having all the relationships of (11), and after some manipulations, the no limit cycles criterion can be expressed as

$$\frac{V_{1,\mathrm{MPP}}}{I_{1,\mathrm{MPP}}} \times 2CV_{2,\mathrm{MPP}} \times \mathrm{TB}f_{\mathrm{DCO}}^2 < \Delta. \tag{14}$$

The result of (14) forms the selection tradeoff between the minimum frequency step that is generated and the deviation Δ from the true MPP. It implies that in a similar way as in other switch-mode applications, the existence of limit cycle oscillations depends on the command signal generator as well as on the local gain of the converter. However, as opposed to conventional applications where the source has no effect on limit cycles [34], here the characteristics of the PV element also contribute a gain factor to the loop. The tool formed in (14), given the system parameters, may assist in the selection of Δ and $\Delta f_{\max}$ in (10) that will allow rapid convergence to the MPP as well as a tolerable steady-state error.

D. Verification by Simulation

To demonstrate the operation of the new DPP and the advanced HC MPPT algorithm, a PSIM (Powersim Inc., ver. 9.0) simulation test bench has been constructed as shown in Fig. 2, with $N = 3$. The HC MPPT algorithm, shown in Fig. 8, has been implemented using a C block element in the PSIM environment. A load resistance value, R_{Load}, that mimics the operation of the central inverter, provides the global MPP according to

$$R_{\mathrm{Load}} = \frac{\left(\sum V_{i,\mathrm{MPP}}\right)^2}{\sum P_{i,\mathrm{MPP}}} \tag{15}$$

where $V_{i,\mathrm{MPP}}$ and $P_{i,\mathrm{MPP}}$ are the PV_i elements' corresponding MPP voltage and power. The resonant power stage elements' values were $C = 1\ \mu$F, $L = 1\ \mu$H, and $R_s = 16\ \mathrm{m}\Omega$. The ZEB size was set at $\Delta = 0.05$. The results shown in Fig. 9 reveal an MPP dc error of 0.55 W (<0.5% of its $P_{i,\mathrm{MPP}}$)

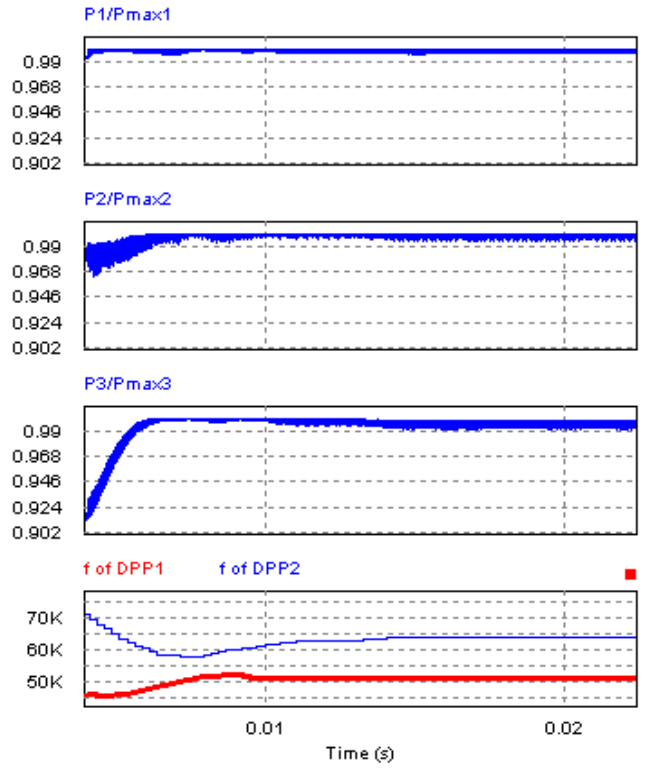

Fig. 9. Simulation results of three PV panels with two DPPs, demonstrating convergence to the MPP. Top three curves: normalized panel power (to its maximum power). Bottom: operating frequency of the DPPs.

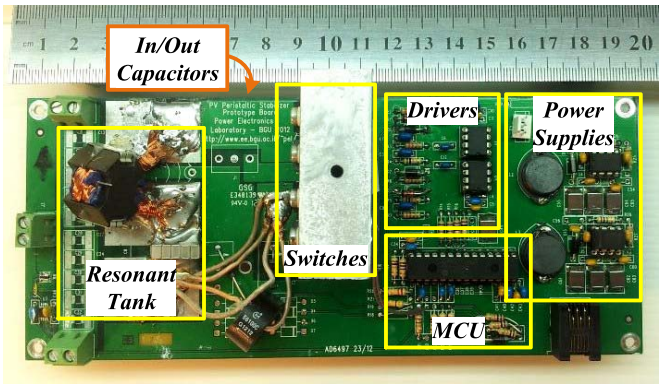

Fig. 10. Photograph of the PCB for the GRSCC converter.

TABLE II
PROTOTYPE PARAMETERS FOR THE THREE CONDUCTED EXPERIMENTS

	L	C	C_B	Δ	MOSFETs	P_{max}	f_{max}	η_{max}
Exp. 1	0.5uH, Ferroxcube RM-8 3F3, A_P=1508×10^{-12}m^4 n=2, ~1mm gap	10×0.1uF, ceramic	5×10uF, ceramic	0.14	PMOS: IXTP96P085T	150W	130kHz	91%
Exp. 2,3		5×0.1uF, ceramic	10×10uF, ceramic	0.1	NMOS: IXTP160N10T	120W	200kHz	93%

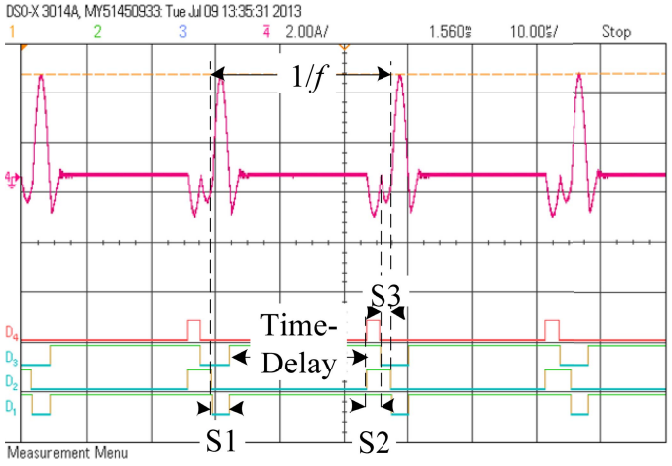

Fig. 11. Experimental results of the L–C tank current and gating signals when processing 1.25 A at $f = 35.8$ kHz.

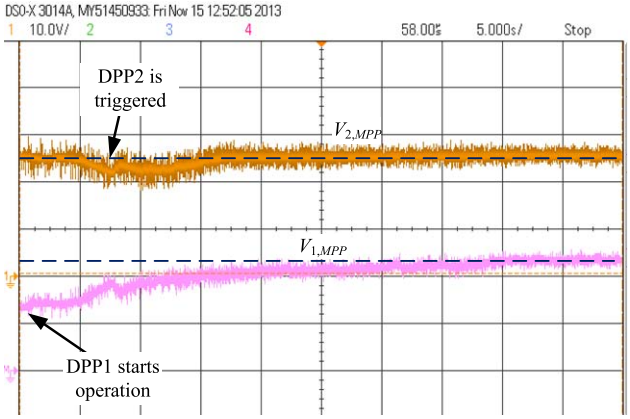

Fig. 12. Experimental results showing convergence to the MPP of the entire string of three panels with two DPPs. Top: voltage of PV1 (10 V/div). Bottom: voltage of PV2 (10 V/div). Horizontal scale: 5 s/div.

without limit cycle oscillations and convergence within 23 iterations.

V. EXPERIMENTAL SYSTEM AND RESULTS

The operation of the differential power architecture has been verified through three independent experiments, the first experiment carried out on a mini chain of three PV panels to verify the theoretical analysis, the second experiment exemplified the operation on a full scale grid connected string and ten panels, and the third one was done to compare the operation of a RSCC to the GRSCC. The GRSCC-based DPP prototypes that were used for the experiments with their specifications enlisted in Table II. The prototypes (Fig. 10) were realized using an inverting bridge configuration, as shown in Fig. 1, using PMOS transistors for Q_1 and Q_3 and NMOS for Q_2 and Q_4. The switches were driven by low-side drivers (MIC4427YN), followed by a passive dc level-shifters for proper gate driving signals, thoroughly discussed in [35]. Adaptive ZCS and HC MPPT algorithms were implemented digitally on a dsPIC33FJ16GS502. The value of the error window, Δ, was selected based on the criterion formed in (13) with some error margin due to the tolerance of the practical parameters. The output voltage ripple was measured to be 1.35 V, which is in a very good agreement with the theoretical calculation of (5).

The first experiment was conducted on a string of three 180-W SHARP PV panels (NU-180, E1). The string was connected to a load to manually seek the string MPP. Two DPP prototypes were connected to the string to enable local MPPT. Fig. 11 shows the inductor's current and the gating signals for one DPP transferring differential current of 1.25 A, for a case of an MPP difference of 38% between two adjacent panels. It also shows the added time delay that controls the average current and the effectiveness of the adaptive ZCS calibration. Fig. 12 shows the convergence of the lower panel toward MPP, within a three PV elements string containing two DPPs. The transient was created by switching on its corresponding DPP, while the second DPP was connected and running, keeping its panel in MPP. Table III summarizes the results of several nonuniform shading conditions and the harvesting factor, ξ(2), for each experiment, and compares between the operation with and without the DPPs. Fig. 13 shows a picture of the testing environment.

The second experiment was conducted on a string of ten 245-W SHARP PV panels (ND-R245A5) connected to an

TABLE III
HARVEST IMPROVEMENT DUE TO ADDITION OF THE DPPS

$P_{1,MPP}$[a]	$P_{2,MPP}$[a]	$P_{3,MPP}$[a]	P_{max}	ξ_{diodes}[b]	ξ_{DPP}[c]	Improv.
0.5	0.95	1	340	0.78	0.94	21%
0.4	0.95	1	327	0.82	0.9	9.3%
0.42	0.74	1	237	0.68	0.96	42%
0.86	1		233	0.94	0.99	5%
0.65	1		200	0.82	0.97	18%
0.54	1		203	0.81	0.95	17%
0.38	1		193	0.68	0.91	33%

a. Normalized to the power of the strongest panel
b. ξ with central inverter only
c. ξ with DPP and a central inverter

TABLE IV
MPP CONDITIONS AND DIFFERENTIAL POWER DEMANDS FOR THE TESTED STRING

	PV_1	PV_2	PV_3	PV_4	PV_5	PV_6	PV_7	PV_8	PV_9	PV_{10}	**Total**
V_{mpp} **[V]**	26.7	26.7	26.7	26.7	32.3	26.7	30.2	26.7	26.7	26.7	276
I_{mpp} **[A]**	6.27	6.27	6.27	6.27	1.97	6.27	4.11	6.27	6.27	6.27	5.53
P_{mpp} **[W]**	167	167	167	167	64	167	124	167	167	167	1530
P_{diff} **[W]**	-20	-40	-59	-79	36	16	59	40	20		368

TABLE V
RESULTS FOR THE TESTED STRINGS

String	V_{PV1}	V_{PV2}	V_{PV3}	V_{PV4}	V_{PV5}	V_{PV6}	V_{PV7}	V_{PV8}	V_{PV9}	V_{PV10}	V_O	I_O	P_O	ξ
control	32	32	32	32	8.5	32	32	32	32	32	297	3.4	1010	66%
DPPs	27.5	27.5	28	27.5	32	27	24	30	29	28.8	281	4.6	1310	86%

Fig. 13. Photograph of the first outdoor experiment. Beer-sheva, Israel. Friday, November 15, 2013.

inverter (ND-R245A5) using nine DPP prototypes. Two panels in the string were partially shaded as observed in Fig. 14. A second independent string with the same shading conditions, connected to a second inverter was also existent as control, lacking the DPPs. The test conditions were at an ambient temperature of 16 °C and irradiation of ∼500 W/m^2. Table IV describes each panel's MPP conditions and the differential power that should be processed to/from the panel.

The table shows substantial difference both in the MPP voltage and MPP current for panels of different shading levels, demonstrating the demand for a DPP that has step-up/down capabilities. Table V shows the measured results of the two strings (DPP connected and control) in operation.

The table shows that using the experimental DPPs aided in extracting an extra 300 W. The power loss due to conversion, estimating a practical efficiency of around 90%, is assumed to be roughly 50 W. This leads to estimated losses of about 170 W due to algorithm mismatch. All the panels can be seen near their MPP voltage with a mismatch of 1–2 V, except PV_7. The small mismatch of the panels' voltages is assumed to be from the existence of Δ, stopping the MPPT near, but not at, the MPP.

TABLE VI
COMPARISON OF THE EXTRACTED POWER USING NO DPP, RSCC, AND GRSCC

String	P_O **[W]**	ξ
no DPP	1579	79%
RSCC	1789	88%
GRSCC	1809	90%

The large mismatch of PV_7 can be from a second local MPP located at 24 V, caused by the nonuniform shading upon the panel or caused by a power trap that imitates local maximum power points [36]. In the third experiment, conducted in March 12, 2014, a comparison between DPPs operating as RSCC, GRSCC, and without DPPs, has been carried out. The PV array has been subjected to shading on the same panels as in experiment 2, but with more moderate shading on PV5 (one filter sheet instead of five) to allow comparability with RSCC operation. Table VI shows the power that was harvested for the three harvesting methods.

The GRSCC-based DPP method has been found to be superior to the conventional RSCC approach even under test conditions of moderate and singular differences between the panels. The results would further be toward the GRSCC method in cases of heavier shadings or if more mismatches exist along the string. In addition, further tuning of the parameter Δ and increasing the accuracy of the measurements would result in better convergence toward the MPP, these will be addressed in future publications.

VI. CONCLUSION

An enhanced differential power processing converter for PV systems was presented. The new power converter combines virtues of both switched-capacitor and switched-inductor technologies, and features low-volume and high-conversion efficiency over wide range. Although based on SCC architecture, the power module is fully capable of performing local MPPT such that only the mismatch power between PV elements is processed, while converging each of the elements into their MPP.

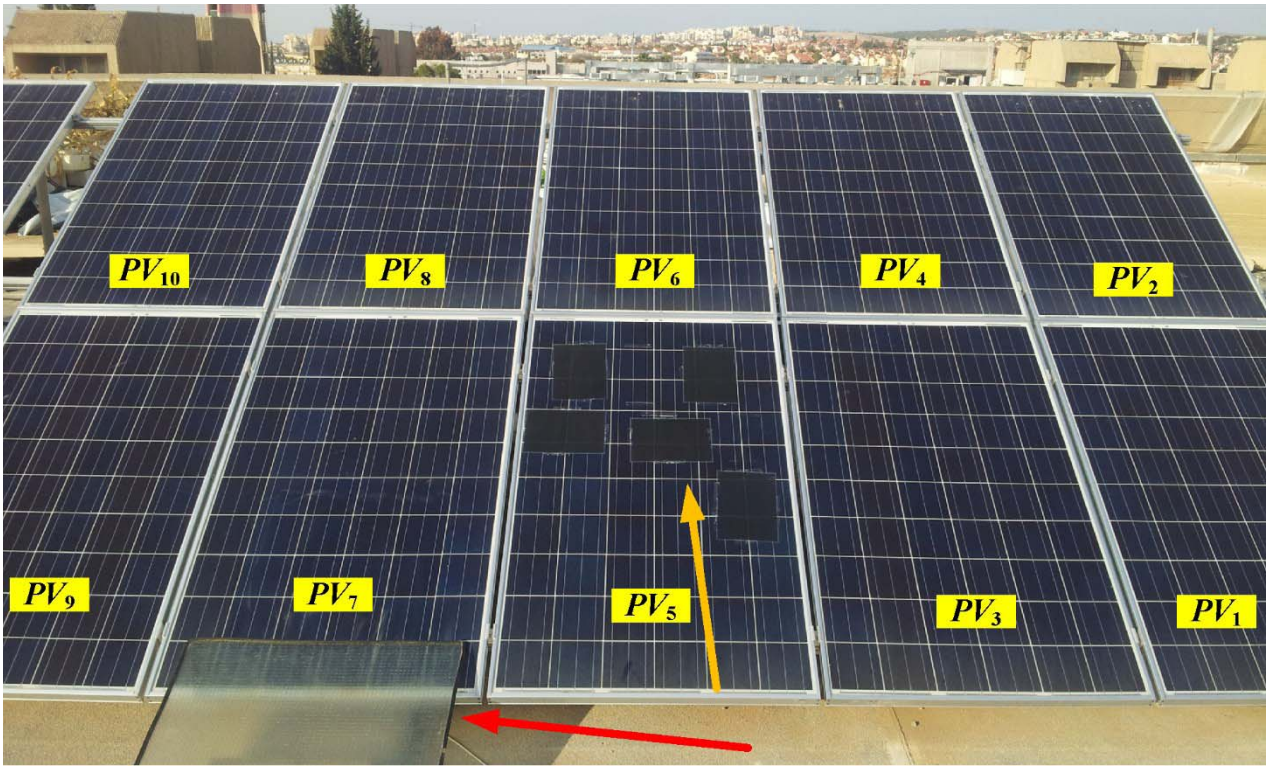

Fig. 14. Photograph of the second outdoor experiment. Beer-sheva, Israel. Sunday, January 16, 2014. PV_5 has five A4-sized filters with opacity of 40%, PV_7 has a diffused glass screen, reducing the irradiation to ∼75%.

A digital differential control scheme was developed and validated. The algorithm design and analysis considers the discrete nature of digital control and eliminates limit cycle oscillations.

A theoretical analysis on the existence of limit cycle oscillations has been carried out. It revealed that deviation from the MPP can be the result of steady-state oscillations around the maximum point due to the finite resolution of the digital hardware, and therefore less energy is extracted. It was also found that the contributors to the oscillations are the frequency resolution of the DCO and the DPP gain around the MPP, and more importantly that the source, the PV element, also has a dominant factor in the appearance of such oscillations. This is contrary to other, conventional, switch-mode applications where the source is assumed as constant. A comparison of ten PV chain harvested with the conventional RSCC and the presented GRSCC approach has been carried out and found it superior in terms of the energy harvesting capability. Future effort to improve the power harvest will consider improvement of the algorithm of steady-state stability as well as a hybrid RSCC–GRSCC approach (can be realized using the same converter topology) that will trigger GRSCC operation only at cases where large voltage difference exists or high-differential power is to be processed.

The experimental results demonstrate significant improvement of power harvesting capability up to 42% for a mini string of only three PV panels (translates into 65 W), and 30% for a ten PV string (translates into 300 W).

Subpanel utilization would increase power harvest capabilities, covering nonuniform shading scenarios within a PV panel, more efficiently [37], [38]. The power processor introduced in this paper, is considered an extremely attractive candidate for subpanel and even cell-level implementation due to its low-volume requirements.

REFERENCES

[1] H. Patel and V. Agarwal, "MATLAB-based modeling to study the effects of partial shading on PV array characteristics," *IEEE Trans. Energy Convers.*, vol. 23, no. 1, pp. 302–310, Mar. 2008.

[2] C. Deline, "Partially shaded operation of a grid-tied PV system," in *Proc. IEEE Photovoltaic Specialists Conf. (PVSC)*, Jun. 2009, pp. 1268–1273.

[3] J. J. Cooley and S. B. Leeb, "Per panel photovoltaic energy extraction with multilevel output DC-DC switched capacitor converters," in *Proc. 26th Annu. IEEE Appl. Power Electron. Conf. Exposit. (APEC)*, Mar. 2011, pp. 419–428.

[4] L. Linares, R. W. Erickson, S. MacAlpine, and M. Brandemuehl, "Improved energy capture in series string photovoltaics via smart distributed power electronics," in *Proc. 24th Annu. IEEE Appl. Power Electron. Conf. Exposit. (APEC)*, Feb. 2009, pp. 904–910.

[5] B. Burger, B. Goeldi, S. Rogalla, and H. Schmidt, "Module integrated electronics—An overview," in *Proc. 25th Eur. Photovoltaic Solar Energy Conf. Exhibit.*, Sep. 2010, pp. 3700–3707.

[6] T. Shimizu, M. Hirakata, T. Kamezawa, and H. Watanabe, "Generation control circuit for photovoltaic modules," *IEEE Trans. Power Electron.*, vol. 16, no. 3, pp. 293–300, May 2001.

[7] Y. Nimni and D. Shmilovitz, "A returned energy architecture for improved photovoltaic systems efficiency," in *Proc. IEEE Int. Symp. Circuits Syst. (ISCAS)*, Jun. 2010, pp. 2191–2194.

[8] R. Kadri, J. Gaubert, and G. Champenois, "Centralized MPPT with string current diverter for solving the series connection problem in photovoltaic power generation system," in *Proc. Int. Conf. Clean Electr. Power (ICCEP)*, Jun. 2011, pp. 116–123.

[9] M. Kasper, D. Bortis, and J. W. Kolar, "Classification and comparative evaluation of PV panel-integrated DC-DC converter concepts," *IEEE Trans. Power Electron.*, vol. 29, no. 5, pp. 2511–2526, May 2014.

[10] P. S. Shenoy, K. A. Kim, B. B. Johnson, and P. T. Krein, "Differential power processing for increased energy production and reliability of photovoltaic systems," *IEEE Trans. Power Electron.*, vol. 28, no. 6, pp. 2968–2979, Jun. 2013.
[11] S. W. Moore and P. J. Schneider, "A review of cell equalization methods for lithium ion and lithium polymer battery systems," in *Proc. SAE World Congr.*, 2001.
[12] K. Sano and H. Fujita, "A resonant switched-capacitor converter for voltage balancing of series-connected capacitors," in *Proc. IEEE Int. Conf. Power Electron. Drive Syst.*, Nov. 2009, pp. 683–688.
[13] S. Ben-Yaakov, A. Blumenfeld, and A. Cervera, "Design and evaluation of a modular resonant switched capacitors equalizer for PV panels," in *Proc. IEEE Energy Convers. Congr. Exposit. (ECCE)*, Sep. 2012, pp. 4129–4136.
[14] J. T. Stauth, M. D. Seeman, and K. Kesarwani, "Resonant switched-capacitor converters for sub-module distributed photovoltaic power management," *IEEE Trans. Power Electron.*, vol. 28, no. 3, pp. 1189–1198, Mar. 2013.
[15] A. Cervera and M. M. Peretz, "Resonant switched-capacitor voltage regulator with ideal transient response," in *Proc. 29th Annu. IEEE Appl. Power Electron. Conf. Exposit. (APEC)*, Mar. 2014, pp. 867–872.
[16] V. V. R. Scarpa, G. Spiazzi, and S. Buso, "Low complexity MPPT technique exploiting the effect of the PV cell series resistance," in *Proc. 23rd Annu. IEEE Appl. Power Electron. Conf. Exposit. (APEC)*, Feb. 2008, pp. 1958–1964.
[17] D. L. King, W. E. Boyson, and J. A. Kratochvil, "Photovoltaic array performance model," Dept. Photovoltaic Syst. R&D, Sandia Nat. Lab., Albuquerque, NM, USA, Tech. Rep. SAND2004–3535, 2004.
[18] G. R. Walker, J. Xue, and P. Sernia, "PV string per-module maximum power point enabling converters," in *Proc. Australasian Univ. Power Eng. Conf.*, Christchurch, New Zealand, Sep./Oct. 2003, pp. 112–117.
[19] G. R. Walker and J. C. Pierce, "Photovoltaic DC-DC module integrated converter for novel cascaded and bypass grid connection topologies—Design and optimisation," in *Proc. 37th IEEE Power Electron. Specialists Conf.*, Jun. 2006, pp. 1–7.
[20] A. Cervera, M. Evzelman, M. M. Peretz, and S. Ben-Yaakov, "A high efficiency resonant switched capacitor converter with continuous conversion ratio," in *Proc. IEEE Energy Convers. Congr. Exposit. (ECCE)*, Sep. 2013, pp. 4969–4976.
[21] S. Ben-Yaakov and M. Evzelman, "Generic and unified model of switched capacitor converters," in *Proc. IEEE Energy Convers. Congr. Exposit. (ECCE)*, Sep. 2009, pp. 3501–3508.
[22] M. Evzelman and S. Ben-Yaakov, "Average-current based conduction losses model of switched capacitor converters," *IEEE Trans. Power Electron.*, vol. 28, no. 7, pp. 3341–3352, Jul. 2013.
[23] M. D. Seeman and S. R. Sanders, "Analysis and optimization of switched capacitor DC-DC converters," *IEEE Trans. Power Electron.*, vol. 23, no. 2, pp. 841–851, Jul. 2008.
[24] J. W. Kimball and P. T. Krein, "Analysis and design of switched capacitor converters," in *Proc. 20th Annu. IEEE Appl. Power Electron. Conf. Exposit. (APEC)*, Mar. 2005, pp. 1473–1477.
[25] K. Kesarwani, R. Sangwan, and J. T. Stauth, "4.5 A 2-phase resonant switched-capacitor converter delivering 4.3 W at 0.6 W/mm^2 with 85% efficiency," in *IEEE Int. Solid-State Circuits Conf. Dig. Tech. Paper*, Feb. 2014, pp. 86–87.
[26] M. Ehsani, I. Husain, and M. O. Bilgic, "Power converters as natural gyrators," *IEEE Trans. Circuits Syst. I, Fundam. Theory Appl.*, vol. 40, no. 12, pp. 946–949, Dec. 1993.
[27] S. Singer, "Gyrators application in power processing circuits," *IEEE Trans. Ind. Electron.*, vol. IE-34, no. 3, pp. 313–318, Aug. 1987.
[28] M. M. Peretz and S. Ben-Yaakov, "Digital control of resonant converters: Enhancing frequency resolution by dithering," in *Proc. 24th Annu. IEEE Appl. Power Electron. Conf. Exposit. (APEC)*, Feb. 2009, pp. 1202–1207.
[29] E. Hamo, A. Cervera, and M. M. Peretz, "Multiple conversion ratio resonant switched capacitor converter with active zero current detection," in *Proc. IEEE Energy Convers. Congr. Exposit. (ECCE)*, Sep. 2013, pp. 805–812.
[30] E. Rotman and S. S. Ben-Yaakov, "Rapid push-pull resonant charger for high power high voltage application using low input voltage," in *Proc. IEEE Energy Convers. Congr. Exposit. (ECCE)*, Sep. 2013, pp. 2325–2332.
[31] T. Esram and P. L. Chapman, "Comparison of photovoltaic array maximum power point tracking techniques," *IEEE Trans. Energy Convers.*, vol. 22, no. 2, pp. 439–449, Jun. 2007.
[32] X. Weidong and W. G. Dunford, "A modified adaptive hill climbing MPPT method for photovoltaic power systems," in *Proc. IEEE 35th Annu. Power Electron. Specialists Conf.*, Jun. 2004, pp. 1957–1963.
[33] C. Schaef and J. T. Stauth, "Multilevel power-point-tracking for variable-conversion-ratio photovoltaic ladder converters," in *Proc. IEEE 14th Workshop Control Model. Power Electron. (COMPEL)*, Jun. 2013, pp. 1–7.
[34] M. M. Peretz and S. Ben-Yaakov, "Digital control of resonant converters: Resolution effects on limit cycles," *IEEE Trans. Power Electron.*, vol. 25, no. 6, pp. 1652–1661, Jun. 2010.
[35] A. Blumenfeld, A. Cervera, and S. Ben-Yaakov, "Analysis and design of DC-isolated gate drivers," in *Proc. IEEE 27th Convers. Electr. & Electron. Eng. Israel*, Nov. 2012, pp. 1–5.
[36] D. C. Jones and R. W. Erickson, "Probabilistic analysis of a generalized perturb and observe algorithm featuring robust operation in the presence of power curve traps," *IEEE Trans. Power Electron.*, vol. 28, no. 6, pp. 2912–2926, Jun. 2013.
[37] S. M. MacAlpine, R. W. Erickson, and M. J. Brandemuehl, "Characterization of power optimizer potential to increase energy capture in photovoltaic systems operating under nonuniform conditions," *IEEE Trans. Power Electron.*, vol. 28, no. 6, pp. 2936–2945, Jun. 2013.
[38] R. C. N. Pilawa-Podgurski and D. J. Perreault, "Submodule integrated distributed maximum power point tracking for solar photovoltaic applications," *IEEE Trans. Power Electron.*, vol. 28, no. 6, pp. 2957–2967, Jun. 2013.

Alon Blumenfeld (S'12) was born in Haifa, Israel, in 1984. He received the B.Sc. degree in electrical and computer engineering from the Ben-Gurion University of the Negev, Beersheba, Israel, in 2011, where he is currently pursuing the M.Sc. degree.

He is an Analog Circuitry Designer of the Research and Development Group in the military industry. His current research interests include photo-voltaic systems, MPPT techniques, switch mode power supplies, and digital control.

Alon Cervera (S'12) was born in London, U.K., in 1985. He received the B.Sc. and M.Sc. degrees in electrical and computer engineering from the Ben-Gurion University of the Negev, Beersheba, Israel, in 2011 and 2013, respectively, where he is currently pursuing the Ph.D. degree in electrical and computer engineering.

His current research interests include switched-capacitor converters, voltage regulation techniques, renewable energy systems, and digital control.

Mor Mordechai Peretz (S'05–M'12) was born in Beersheba, Israel, in 1979. He received the B.Tech. degree in electrical engineering from the Negev Academic College of Engineering, Beersheba, in 2003, and the M.Sc. and Ph.D. degrees in electrical and computer engineering from the Ben-Gurion University of the Negev, Beersheba, in 2005 and 2010, respectively.

He was a Post-Doctoral Fellow with the Laboratory for Power Management and Integrated SMPS, University of Toronto, Toronto, ON, Canada, from 2010 to 2012. In 2012, he joined the Department of Electrical and Computer Engineering, Ben-Gurion University of the Negev, where he is currently the Director of the Power Electronics Laboratory. His current research interests include digital and smart control methods for efficient energy processing, SMPS miniaturization, mixed-signal IC design of SMPS, modeling and computer-aided design, applications of nonlinear magnetics, and renewable energy systems.